Experimental deformation of a single-layer anhydrite in halite matrix under bulk constriction. Part 1: Geometric and kinematic aspects

G. Zulauf [a,*], J. Zulauf [a], O. Bornemann [b], N. Kihm [c], M. Peinl [a], F. Zanella [c]

[a] Institut für Geowissenschaften, Universität Frankfurt a.M., Altenhöferallee 1, D-60438 Frankfurt a.M., Germany
[b] Bundesanstalt für Geowissenschaften und Rohstoffe, Stilleweg 2, D-30655 Hannover, Germany
[c] Institut für Neuroradiologie, Universität Frankfurt a.M., Theodor-Stern-Kai 7, 60596 Frankfurt a.M., Germany

ARTICLE INFO

ABSTRACT

A new deformation apparatus has been used to model the internal kinematics of salt diapirs. Composite natural samples consisting of a single layer of anhydrite, embedded in halite matrix, were constrictionally deformed at temperature, $T = 345\,^\circ C$, strain rate, $\dot{e} = 10^{-7}\,s^{-1}$, maximum viscosity, $\eta = 2 \times 10^{13}$ Pa s, and maximum finite strain, $e_x = 122\%$. The anhydrite layer, oriented parallel to the major stretching axis, X, was deformed by fracturing, whereas halite behaved viscously. At advanced state of constriction ($e_x > 90\%$) a strong increase in strain hardening of halite led to a transient tension fracture that healed up and was shortened by folding during the final phase of viscous deformation.

Tiny prismatic anhydrite inclusions disseminated inside the halite matrix were reoriented during constriction resulting in a linear grain-shape fabric. 3D-images of the anhydrite layer, based on computer tomography, revealed rare kink folds with axes subparallel to X, and boudins which result from tension fracture. With increasing layer thickness, H_i, the width of boudins, W_a, increases linearly ($W_a = -0.3 + 1.3 \times H_i$). The normalized width of boudins ($W_d = W_a/H_i$) is almost constant at 1.5 ± 1.0. These geometrical parameters can be used to reveal fracture boudinage under bulk constriction. The oblique orientation of most of the boudins, with respect to the principal strain axes, results from folding of the boudins by a second generation of folds, the latter with axes subperpendicular to the layer.

1. Introduction

Salt diapirs are important for the storage of hazardous waste, the exploitation and mining of rock salt, and petroleum exploration and storage. Seismic exploration, deep drilling, and gravity surveys have provided accurate details on the shape and deformation of many salt diapirs. However, although deformation structures in the internal parts of salt diapirs are known for a long time (e.g. Posepny, 1871; Stille, 1925), their origin is only poorly understood because these structures are notoriously complex and require investigation in three dimensions (Jackson, 1995). Mushroom diapirs are characterized by crescentic folds in horizontal section and by downward facing folds in vertical section (Jackson and Talbot, 1987). The internal parts of salt stocks are characterized by steeply plunging linear (L > S) fabrics, examples of which are present in the salt domes of northern Germany (Lotze, 1957, and references therein), the Grand Saline Dome of Texas (Balk, 1949) and the Jefferson Island, Avery Island, Weeks and Winnfield Dome in Louisiana (Rogers, 1918; Balk, 1953; Hoy et al., 1962). Near the core of the Upheaval Dome in Utah, radial shortening produced constrictional bulk strain, forming an inward verging thrust duplex and tight to isoclinal, circumferentially trending folds (Jackson et al., 1998).

The youngest folds recognized in stems of salt diapirs are known from German Zechstein salt as curtain folds (Stier, 1915; Hartwig, 1925; Lotze, 1957, Fig. 176b; Trusheim, 1960; Zirngast, 1996) because the steeply inclined bedding planes define steeply plunging cylindrical folds with steeply dipping curved axial surfaces. In a horizontal section of a salt stock the axial planes of curtain folds are generally radial and the envelope is more or less concentric. Based on experiments by Torrey and Fralich (1926), curtain folds were experimentally produced by pressure forcing a ductile stratified sequence through a circular vent in a brittle overburden (Escher and Kuenen, 1929).

The modeling results of Ramberg (1981) suggest constrictional flow in the basal parts of axisymmetric diapirs. Thus, only curtain folds with steep hinges, aligned parallel to the subvertical X-axis of the finite strain ellipsoid, are likely to be generated in the basal parts of diapiric stems. In cases of rheological stratification (e.g. stiff anhydrite or shale layers embedded in a weaker halite matrix), the curtain folds should be associated with boudins, the latter resulting

* Corresponding author.
E-mail address: g.zulauf@em.uni-frankfurt.de (G. Zulauf).

from vertical extension parallel to the steep axes of the curtain folds. Examples of folded and boudinaged anhydrite layers, embedded in a steep prolate halite matrix, have been described from Miocene salt diapirs of Yemen (Davison et al., 1996a, b). Modeling of salt diapirs using rock analogues has further shown that competent layers like anhydrite could be subjected to boudinage before being entrained and constrictionally deformed in the stem of the salt diapir (Koyi, 2001).

The 3D-geometry, flow lines and distribution of finite strain within an idealized axisymmetrical salt stock have been illustrated by Talbot and Jackson (1987). All the stream tubes in the lower half of the stem converge upward. The strain near the central axis is characterized by pure constriction supporting linear fabrics and related L-tectonites. Apart from these idealized axisymmetric salt stocks, there are other types in nature showing different shape and internal structure. The shape of a diapir and the amount of entrainment and distribution of initially interbedded dense layers are strongly controlled by salt supply which depends on sedimentation rate, viscosity of salt, perturbation width, and initial stratigraphic position of the embedded anhydrite layer (Chemia et al., 2008; Chemia and Koyi, 2008).

Constrictional experiments on pure natural rock salt have been carried out by Skrotzki and Welch (1983) focusing on the crystallographic preferred orientation of halite. Experimental studies on composite salt rocks (e.g. layer(s) of clay or anhydrite in halite matrix), however, are lacking. Such types of experiments are restricted to rheologically stratified rock analogues (plasticine). They have shown that both folds and boudins may grow simultaneously under pure constriction (Kobberger and Zulauf, 1995; Zulauf et al., 2003; Zulauf and Zulauf, 2005).

In the present paper we present details about a new deformation rig that was used for constrictional thermomechanical experiments of natural rocks. It will be shown how boudins and folds develop in a single anhydrite layer that is embedded in a viscous halite matrix. We are focusing particularly on the geometry of growing instabilities and on rheological aspects. With exception of the starting samples, the microfabrics of deformed halite and anhydrite are not considered in the present article because of limited printing space. The results of microfabric studies will be published separately in a companion paper.

2. Experimental setup

2.1. Selection, production and preparation of samples

A major problem of the present project was to find appropriate samples consisting of an anhydrite layer which is embedded in halite matrix. There are three possibilities to obtain such samples: (1) natural samples in which anhydrite is already sandwiched in halite matrix; (2) synthetic composite samples made of natural anhydrite and natural halite; (3) preparation of composite samples using synthetic material.

Natural samples of halite with a layer of anhydrite are available and thus could be used in principle. Examples from the borehole Teutschenthal (Germany) have been used when carrying out first experiments to calibrate and test the new machine. However, the anhydrite layer of such samples is in most cases already deformed by folding or boudinage. This holds particularly for cases where the anhydrite layer is thin (which is also the case in our experiments). Another problem of natural anhydrite–halite samples is the fact that the upper and lower interface of both phases can be different (e.g. sharp contact at one interface and gradual contact at the other interface). In this case the interpretation of experimental data will be more difficult. Entirely synthetic samples have the disadvantage that they may differ significantly from natural samples (e.g. in grain

size, grain shape, amount of impurities, fluid inclusions, etc.). Because of these reasons we decided to build composite samples using natural halite as matrix and natural anhydrite as layer (Fig. 1a). All samples were delivered by BGR Hannover.

Halite samples of the Asse borehole of northern Germany (800 m level, Speisesalz Na2SP) which are – with one exception – largely free from a grain-shape fabric (SPO) show the lowest degree of mechanical anisotropy under constriction and thus have been used for the experiments. The grain size varies from 2 to 12 mm. According to microscopic and XRD analyses the Speisesalz (Na2SP) used in the present study consists of almost pure halite, with anhydrite and polyhalite ($K_2MgCa_2(SO_4)_4 \times 2H_2O$) as the most important impurity phases. The total water content of other Asse Na2SP samples is 0.05 wt% (Urai et al., 1987). Inclusions of partly twinned anhydrite with grain sizes up to 4 mm are present within the halite grains and along halite grain boundaries. These inclusions do not show a preferred orientation. The microfabrics of Asse halite have been described by Urai et al. (1987). Evidence for dislocation creep is indicated by the presence of crystallographic preferred orientation (Brokmeier, 1983), subgrains and lobate grain boundaries, the latter resulting from strain-induced grain boundary migration (Urai et al., 1987). The fact that most of the high-angle grain boundaries are enriched by opaque phases and inclusions suggests that dissolution–reprecipitation creep operated as a further deformation mechanism. The inclusions are the terminations of a complicated network of grain boundary fluid inclusions which are present on at least 80% of the grain boundaries (Urai et al., 1987; see also Schenk and Urai, 2004).

For the present studies we selected samples of Asse halite, most of which do not show a grain-shape fabric. The anhydrite samples used for our experiments have been collected from the Gorleben deep borehole 1004. XRD analyses revealed impurities of halite, polyhalite and magnesite. The grain size of the samples used varies considerably from <100 μm to 10 mm. Most of these grains have a dirty habitus, the latter resulting from numerous fluid inclusions and opaque phases. Rosette shaped aggregates of anhydrite are frequently present on almost all scales. The anhydrite rosettes are partly truncated by highly lobate seams which are rich in opaque phases. These seams reflect localized dissolution–precipitation creep (see also Bauerle et al., 2000).

Our decision to use composite samples of natural halite and anhydrite for the experiments, led to a serious problem concerning the preparation of such samples. We had to build a halite cube which includes a single layer of anhydrite with interfaces showing strong cohesion similar to that of natural examples. To fit anhydrite slices in-between halite blocks, we carried out more than 15 long-term experiments at different but always wet conditions. The parameters changed were (i) temperature, (ii) degree in saturation of NaCl brine, (iii) pressure, and (iv) nature of the contact surfaces. The right procedure for producing composite halite–anhydrite samples which show interfaces with sufficient cohesion includes the following steps:

- Dry cutting of halite cube ($60 \times 60 \times 60$ mm) into 2 halves and cutting of a reference sample out of the cube (ca. 1/3 of the cube).
- Heating of halite up to 40 °C and dry grinding of surfaces which will be in contact with anhydrite (SIC grain 180).
- Wet cutting and grinding of anhydrite layer (SIC grain 120). If the thickness of the anhydrite layer was <1.5 mm, the layer is prone for buckling. In this case the grinding had to be carried out using SIC grain 240 and a plane plate made of glass.
- Cutting of a reference sample of anhydrite (ca. 1/3 of the layer).
- Immersing of anhydrite and halite into slightly undersaturated NaCl brine for 45 s at room temperature.
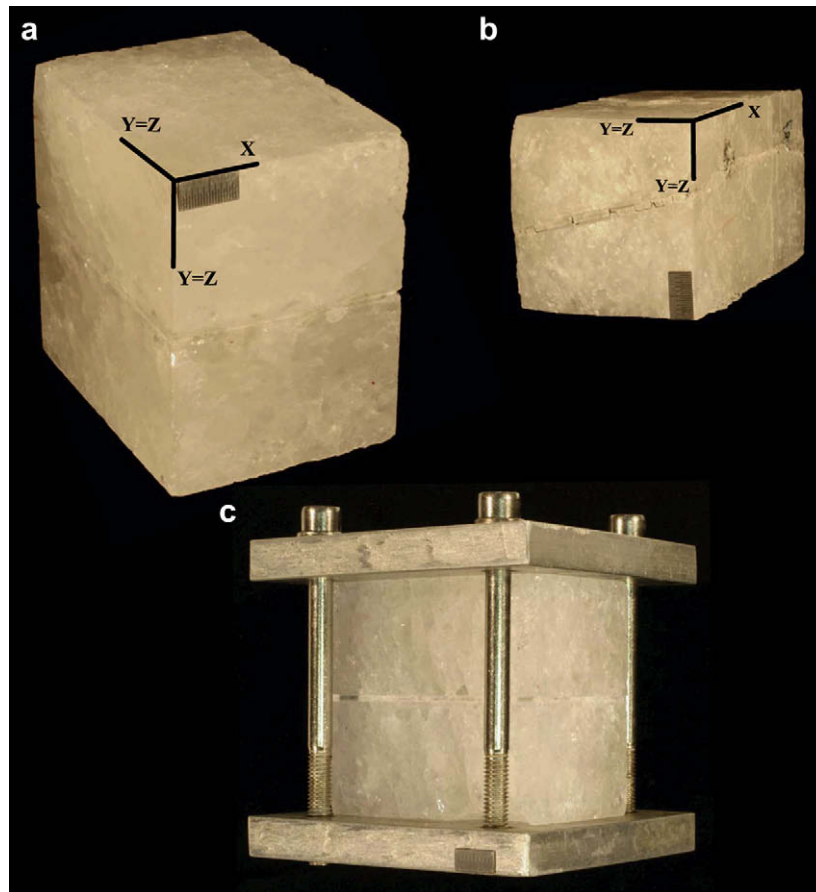
Fig. 1. (a) Initial composite sample of halite matrix with layer of anhydrite. $H_i = 1.5$ mm. (b) Same sample like (a) but deformed under bulk constriction at $T = 345\,^\circ$C and $\dot{e} = 4 \times 10^{-7}\,\mathrm{s}^{-1}$; $e_x = 122\%$; $e_{Y=Z} = -33\%$. (c) Special device for fitting halite matrix and anhydrite layer together. Undeformed sample is squeezed between two plates with the maximum stress perpendicular to the anhydrite layer. Grey scale bar in all cases = 1 cm. For further explanation see text.

- Inserting composite halite–anhydrite sample into a simple press (Fig. 1c) and carefully crosswise tightening of the four screws at room temperature.
- After 48 h slowly heating of sample up to $T = 150\,^\circ$C.
- After 24 h again carefully crosswise tightening of the four screws.
- After additional 24 h slowly decreasing of temperature to room temperature, crosswise loosening of screws and removing composite halite–anhydrite sample from press.

We carried out six runs using composite samples produced by this procedure with anhydrite layers showing the following thicknesses: 0.8 mm, 1.1 mm, 1.5 mm, 1.85 mm, 2.2 mm, and 2.5 mm (Table 1). The uncertainty of the layer thickness is 0.1 mm. In each of the six runs the initial model dimension (halite matrix plus anhydrite layer) was $60 \times 60 \times 43$ mm. The squared face of the sample was oriented perpendicular, and the anhydrite layers were oriented parallel, to the X-axis of the finite strain ellipsoid. A 3D view of a deformed sample is shown in Fig. 1b. The reference sample (ca. 1/3 of the initial cube) was stored for microfabric studies.

2.2. Deformation apparatus and deformation conditions

Deformation of the composite halite–anhydrite samples was performed using a new deformation rig. The basic concept of the new machine is similar to that of the apparatus described in Zulauf et al. (2003). It is supporting the full range of three-dimensional coaxial deformation. However, in contrast to the former one, the new machine is working at higher temperatures and pressures.

The new deformation rig consists of a stable frame made of steel (painted in blue, Fig. 2) in which four principal aluminum plates have been orthogonally assembled (H1–H4 in Fig. 2c,d). The sample is sandwiched between the four plates. Maximum initial model dimensions are $180 \times 180 \times {>}180$ mm (Fig. 2c). Minimum initial model dimensions are $30 \times 30 \times {>}30$ mm (Fig. 2d). Those surfaces of the plates which are in contact with the samples have been reinforced.

Plate H4 is immobile while fixed to the frame. The other plates are moving along sledges. The movement of plates H1 and H2 is performed in each case by a spindle, the latter being driven by two separate three-phase stepping motors via a gear. The maximum torque of the motors is 1200 N cm. The rated power is 0.75 kW$_{\mathrm{eff}}$. The motor speed is variable in the range 1–3000 rpm, and the number of revolutions is adjusted by the control unit (Fig. 2b). The corresponding finite longitudinal strain rates, $\dot{e}$, range from $2 \times 10^{-7}\,\mathrm{s}^{-1}$ to $3 \times 10^{-2}\,\mathrm{s}^{-1}$.

The plates can move in manual or automatic mode. The manual mode implies a fast drive which supports a maximum plate velocity of 100 mm h^{-1}. This mode is used to bring the plates into contact with the sample. If plate H1 is moving to the left, plate H2 will be passively shifted in the same direction (see black arrows in Fig. 2c). Plate H2 can further move actively in the vertical direction if the vertical spindle is driven. During deformation plate H2 is moving

Table 1
Deformation parameters and geometric data obtained from constrictional thermomechanical runs.

Experimental run			K 0.8	Error	K 1.1	Error	K 1.5	Error	K 1.85	Error	K 2.2	Error	K 2.5	Error
Deformation temperature	T	°C	345	0.1	345	0.1	345	0.1	345	0.1	345	0.1	345	0.1
Length of initial sample along X	dX	mm	43	0.5	43	0.5	43	0.5	43	0.5	43	0.5	43	0.5
Length of initial sample along Y	dY	mm	60	0.5	58	0.5	60	0.5	60	0.5	60	0.5	60	0.5
Length of initial sample along Z	dZ	mm	60	0.5	60	0.5	60	0.5	60	0.5	60	0.5	60	0.5
Initial thickness of anhydrite layer	H_i	mm	0.8	0.1	1.1	0.1	1.5	0.1	1.85	0.1	2.2	0.1	2.5	0.1
Finite strain along $Y = Z$	$e_Y = e_Z$		−0.32		−0.33		−0.33		−0.32		−0.33		−0.17	
Finite strain along X	e_x		1.16		1.22		1.22		1.16		1.22		0.44	
Finite longitudinal strain rate	$\dot{e}_{Y=Z}$	s^{-1}	−3.9E − 07		−3.9E − 07		−3.9E − 07		−1.93E − 07		−3.9E − 07		−1.9E − 07	
Maximum stress parallel to layer	$\sigma_{Y=Z//\text{layer (max)}}$	Pa	3.9E + 06		4.0E + 06		4.5E + 06		4.4E + 06		4.6E + 06		4.3E + 06	
Maximum stress perpendicular to layer	$\sigma_{Y=Z \text{ perp. layer (max)}}$	Pa	1.5E + 06		3.9E + 06		4.5E + 06		2.4E + 06		3.9E + 06		2.1E + 06	
Maximum viscosity parallel to layer	$\eta_{Y=Z//\text{layer (max)}}$	Pa s	9.7E + 12		1.0E + 13		1.1E + 13		2.2E + 13		2.3E + 13		2.2E + 13	
Maximum viscosity perpendicular to layer	$\eta_{Y=Z \text{ perp. layer (max)}}$	Pa s	3.7E + 12		9.7E + 12		1.1E + 13		1.2E + 13		1.9E + 13		1.1E + 13	
Finite layer thickness — Based on CT image	H_f	mm	1.1	0.2	1.3	0.1	1.7	0.2	2.1	0.2	2.1	0.2	2.0	0.2
Change in layer thickness ($H_f/H_i \times 100 - 100$) — Based on CT image	ΔH	%	37.5		18.2		13.3		13.5		−4.5		−20.0	
Number of boudins — Based on CT image	N_{Boudin}		25.6	2.3	20.2	2.0	19.3	1.9	16.5	1.1	12.0	2.0	9.9	2.0
Length of boudins — Based on CT image	$W_{a\,(\text{Boudin})}$	mm	0.8	0.4	1.2	0.5	1.5	0.8	2.0	0.9	2.6	1.1	3.0	1.6
Normalized length of boudins (W_a/H_f) — Based on CT image	$W_{d\,(\text{Boudin})}$		0.73	0.44	0.92	0.42	0.88	0.53	0.95	0.474	1.24	0.58	1.50	0.89
Average arc length of folds — Based on CT image	$W_{a\,(\text{fold})}$	mm	15.8	1.8	32.8	2.2	28.8	9.0	28.7	8.0	27.9	7.2		
Normalized arc length of folds (W_a/H_f) — Based on CT image	$W_{d\,(\text{fold})}$		14.4	2.0	25.2	1.8	16.9	6.0	13.7	4.2	13.3	3.8		
Finite layer thickness — Based on common section	H_f	mm	0.78	0.05	1.09	0.05	1.48	0.03	1.91	0.04	2.5	0.1	2.58	0.04
Change in layer thickness ($Hf/Hi \times 100$-100) — Based on common section	ΔH	%	−2.5		−0.9		−1.3		3.2		13.6		3.2	
Number of boudins — Based on common section	N_{Boudin}		31		25		24		17		14		11	
Length of boudins — Based on common section	$W_{a\,(\text{Boudin})}$	mm	1.1	0.5	2.0	0.9	2.3	0.9	2.5	1.0	2.6	0.8	4.1	2.3
Normalized length of boudins (W_a/H_f) — Based on common section	$W_{d\,(\text{Boudin})}$		1.41	0.68	1.8	0.9	1.6	0.6	1.31	0.53	1.0	0.3	1.6	0.9
Post-fracture longitudinal strain — Based on common section	$e_{Y=Z\,(\text{post-fracture})}$		−0.05		−0.08		−0.07		−0.04		−0.08			

upwards. Plate H3 is moving only passively in the vertical direction because of the push imposed by plate H2.

In cases of pure constrictional strain (Flinn parameter $k = \infty$) the number of revolutions of both motors is the same, meaning that plates H1 and H2 are moving with the same velocity. There are two possibilities to produce plane strain ($k = 1$). In one case, plate H1 and associated plate H2 move to the left, whereas plate H3 is immobile. In the other case plate H1 is immobile and plates H2 and H3 move upwards. Similar to the case of constrictional strain, the X-axis of the finite strain ellipsoid is horizontal in both cases of plane strain configuration. There are also two possibilities for pure flattening strain ($k = 0$). Given that sufficient space is initially present between the specimen and plates H2 and H4, respectively, we can push plate H1 towards the left, parallel to the Z-axis of the finite strain ellipsoid. In this case, the equal X- and Y-axes are vertical and horizontal, respectively. In cases where enough space is present between the specimen and plates H1 and H3, we can move plate H2 upwards (that is parallel to Z) to produce pure flattening strain.

To increase the temperature of the plates, the latter are subdivided into 3 zones, each of which contains 4 heating cartridges. The temperature of each plate is measured by 7 thermocouples. At pre-scribed time intervals the temperature values are recorded by the control unit and adjusted to the target value. The heating cartridges support a maximum deformation temperature of 375 °C with an uncertainty of less than 0.1 °C. To hold the temperature constant, isolating plates and felt have been installed. Besides the temperature of each zone, the sample temperature and the room temperature are measured by additional thermocouples and recorded by the control unit (Fig. 2b).

Concerning the temperature evolution during a run, two steps are possible. The first step implies adjustment of (i) starting temperature, (ii) degree in temperature ascent (descent), (iii) target temperature 1, and (iv) duration of target temperature 1. The second step includes (i) target temperature 1, (ii) degree in temperature ascent (descent), and (iii) target temperature 2. Thus, the new machine can be used to deform samples during increasing and decreasing temperatures within one and the same run.

Both the heating and the motors will be switched off automatically if pre-scribed temperature limits are exceeded. Measurements of in-situ stresses allow constraining in-situ viscosities in the direction of the principal strain axes. There are two single-point load cells, each fixed at plates H3 and H4, respectively, and linked with the control unit to determine the horizontal and vertical stresses during deformation. Each load cell shows a maximum nominal load-bearing capacity of 72 kg. As the size of the samples could be large ($180 \times 180 \times >180$ mm), the maximum applied vertical and horizontal stresses have been set at 4.6 MPa.

During an experimental run, the temperature, stress and strain data are recorded for pre-scribed time intervals (3–24 s) and stored in ASCI and/or EXCEL format. Deformation of halite–anhydrite has to be performed at slow strain rates (10^{-7} s^{-1}) resulting in a deformation time of >3 weeks if finite strain is moderate.
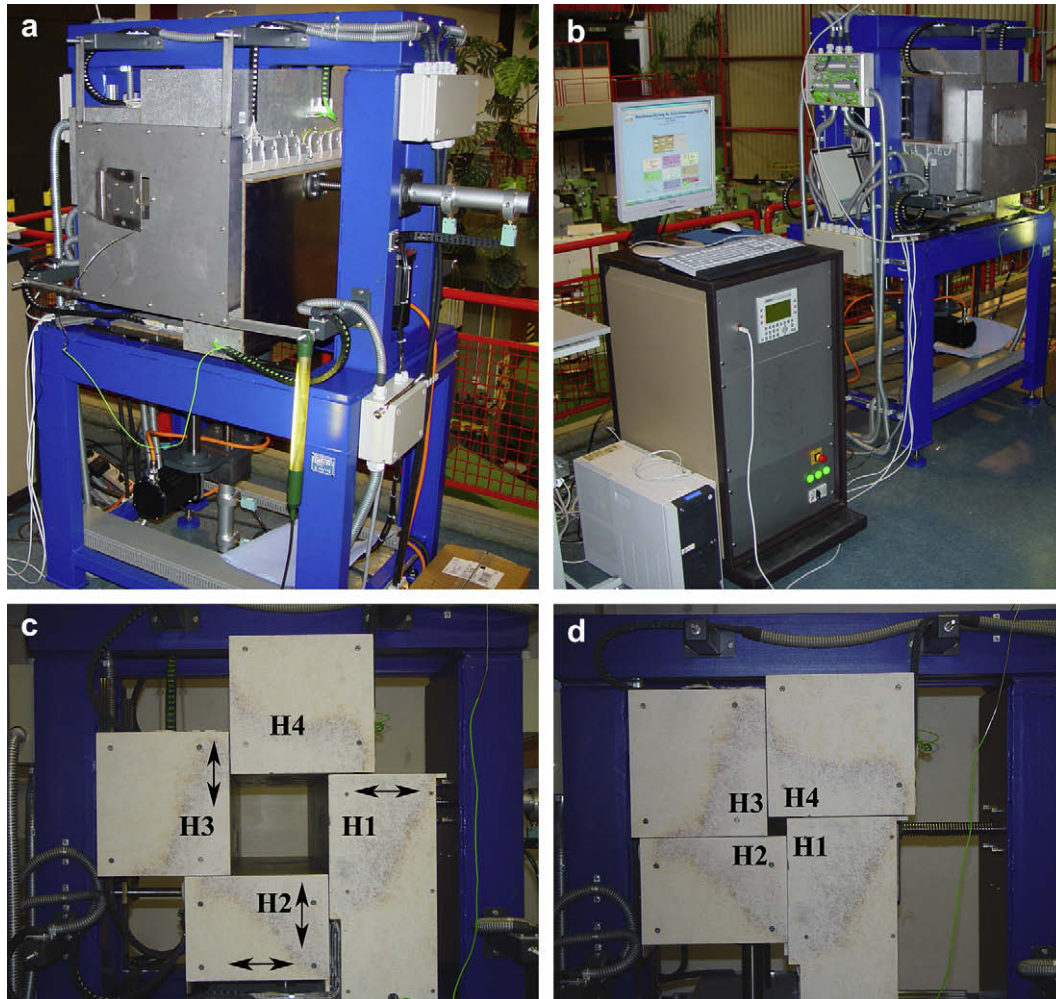
Fig. 2. (a) New deformation apparatus for 3D coaxial deformation at $T = 20$–375 °C, $e = 3 \times 10^{-2}$ s^{-1} to 2×10^{-7} s^{-1}, and $\sigma_{max} = 4.59$ MPa. (b) Control unit. (c) Sample space of deformation apparatus open with maximum distance (180×180 mm) between moving plates; plate H4 is fixed to the blue steel frame; plates H1-H3 are movable as is indicated by black arrows. (d) Sample space with minimum distance (30×30 mm) between the plates. For further explanation see text. (For interpretation of the references to colour in this figure legend, the reader is referred to the web version of this article.)

When putting the halite–anhydrite sample into the sample space of the deformation apparatus, caution is needed. While the sample is heated up from room temperature to $T > 300$ °C, halite will show significant thermal expansion. Thus, sufficient space (more than 20 mm) is needed between the sample and the moving plates before the heating is switched on. To be sure that during deformation the temperature of the sample is the same as the temperature of the plates, the motors of the machine were switched on ca. 12 h after the pre-scribed temperature (345 °C) was reached by the plates. Initial tests with a thermo couple inserted into a sample of halite have shown that after a period of ca. 3 h the difference in temperature between sample and plates is less than 1 °C. Because of the striking large difference in thermal expansion between the halite matrix and the anhydrite layer, the composite sample was heated slowly (20 °C h^{-1}). In cases of fast heating the sample would react by pervasive fracturing.

As halite supports corrosion of the load cell which is made of steel, we used sheets of *Kapton* foil that have been inserted between the stamp and the sample.

In the present case of constrictional experiments the anhydrite layer was oriented parallel to the X-axis of the finite strain ellipsoid. Deformation conditions during the pure constrictional runs were as follows: $T = 345$ °C, $\dot{e} = 2$–4×10^{-7} s^{-1}, $e_{Y=Z} = -33\%$ and $e_x = 122\%$

(Table 1). Only in that run where the initial thickness of the anhydrite layer, H_i, was set at 2.5 mm, the deformation of the sample was limited to a finite strain $e_{Y=Z} = -17\%$ and $e_x = 44\%$, respectively, because the pre-scribed stress limit of the machine was reached (see below). If the pre-scribed finite strain was reached, the motors were stopped and the temperature of the sample was slowly reduced (ca. 20 °C h^{-1}) until room temperature.

2.3. Geometric analysis of deformation structures

Most of the deformed samples have been investigated using computer tomography (CT) and conventional cuts along YZ and $XY = XZ$ sections (for details, see Zulauf et al., 2003). The CT studies were performed at the clinic of Frankfurt University in the Neuroradiologie Department using a multislice spiral CT scanner (Phillips CT Brilliance with 6 lines). As a sufficient contrast in density between anhydrite layer (2.9 g cm^{-3}) and halite matrix (2.1 g cm^{-3}) is given, there is no problem to visualize the deformation structures of the anhydrite layer using CT. When carrying out CT studies conditions for analyzing the halite–anhydrite samples were as follows: slice thickness = 0.8 mm, spacing = 0.6 mm, standard resolution.

Geometrical parameters of folds and boudins have been determined from CT images using the software *Smooth*, which supports

production, visualisation, and analyses of DICOM volumetric data. *Smooth* can be used for 3D reconstructions based on histological sections even if the latter are free from external landmarks. The presentation of data by polygons and voxels allows the combination of polygon models with arbitrary number of sections, the latter with any orientation when cutting through the volumetric data set. These sections can be processed interactively in real time. Complex polygon models can be produced from several less complex polygon models. The models shown on the screen are either transparent or opaque. The visualisation and interpretation of 3D models are significantly improved using a special pseudocolour mode. Apart from central projection, there is a possibility to present the 3D models in parallel projection. The latter type is used when measuring geometric data (length, angle, area) on the screen.

The initial wavelength of folds (W_i sensu Ramsay and Huber, 1987, p. 383) has been determined by measuring the average fold arc lengths (Sherwin and Chapple, 1968; Hudleston, 1973). The normalized initial wavelength W_d is calculated by dividing the initial wavelength through the finite layer thickness H_f. Because of strong boundary effects (see below), geometrical parameters have not been determined from folds and boudins of the marginal parts of the deformed samples.

All geometric parameters like length, angles, etc. have been determined using the image analysis software DIANA.

3. Results

3.1. Stress–strain data

The stress–strain plots of the six runs show striking differences with increasing layer thickness (Fig. 3). Most of these differences can be explained by the fact that the stamp of the load cell, which records the horizontal stress parallel to the layer, was placed on the anhydrite layer, whereas the stamp of the second load cell, which records the vertical stress perpendicular to the layer, was placed on the halite matrix. The stress parallel to the layer is either higher than, or almost the same as the stress perpendicular to the layer. There is a tendency that with increasing layer thickness the difference between horizontal and vertical stresses also increases. One exception is given if H_i was lowest at 0.8 mm. In this case the stress *parallel* to the anhydrite layer is much higher than the stress perpendicular to the layer (Fig. 3a). After an almost linear increase in stress, plastic yielding is achieved at $e_{Y=Z}=$ ca. −10%. However, a steady state does not occur. At higher finite strain there is still strain hardening. The stress *perpendicular* to the anhydrite layer is much smaller. Plastic yielding started at ca. 7% strain and subsequent deformation operated under almost steady-state conditions. At maximum finite strain ($e_{Y=Z}=$ ca. −30%) the viscosity (η) in the direction parallel and perpendicular to the layer was 9.7×10^{12} and 3.7×10^{12} Pa s, respectively (Table 1).

If H_i was set at 1.1 mm, the paths of both flow curves are close to each other (Fig. 3b), meaning that the impact of the stiff anhydrite layer on the mechanical behavior of the sample was weak. The plot shows non-linear flow curves with an initial linear increase of stress and strain until plastic yielding is achieved at $e_{Y=Z}=−3$ and −7%, respectively. Both flow curves do not indicate steady-state behavior, but strain hardening. The latter is particularly strong at advanced finite strain. There is a striking increase in horizontal and vertical stresses at $e_{Y=Z}=$ ca. −25%. After attaining this strain state, both flow curves show the same steep path, the latter reflecting significant strain hardening. At maximum finite strain the viscosity in the direction parallel and perpendicular to the layer was 1.0×10^{13} and 9.7×10^{12} Pa s, respectively.

If H_i was set at 1.5 mm, the flow curves (Fig. 3c) are similar to those described from the previous run. This holds particularly for

the striking increase in horizontal and vertical stresses at advanced finite strain ($e_{Y=Z}=−25$ to −28%). However, plastic yielding along the horizontal direction (parallel to the anhydrite layer) was achieved much later ($e_{Y=Z}=$ ca. −7%) than the yielding along the vertical direction ($e_{Y=Z}=$ ca. −3%). The later onset of plastic yielding in the direction parallel to the anhydrite layer is also given in those runs where the layer thickness was still higher. At maximum finite strain the viscosity in the direction parallel and perpendicular to the layer was almost the same (1.1×10^{13} Pa s, Table 1).

If H_i was set at 1.85 mm the stress parallel and perpendicular to the layer is strikingly different (Fig. 3d). The stress–strain data obtained *parallel to the layer* show plastic yielding at $e_{Y=Z}=$ ca. −7% at a stress difference of ca. 3.3 MPa. After plastic yielding the deformation continued under steady state until a finite strain $e_{Y=Z}$ of −28% was achieved. Subsequently the degree in strain hardening increased significantly. The stress difference in the direction *perpendicular to the layer* shows a strikingly different behavior with much lower stresses and a less distinct yield point. At maximum finite strain the viscosity in the direction parallel and perpendicular to the layer was 2.2×10^{13} and 1.2×10^{13} Pa s, respectively.

At $H_i = 2.2$ mm the horizontal and vertical flow curves are almost parallel at advanced finite strain magnitudes. However, the stress parallel to the layer is ca. 0.5 MPa higher than the stress perpendicular to the layer (Fig. 3e). The minor change in strain rate from 4×10^{-7} s^{-1} to 2×20^{-7} s^{-1} did not significantly affect the flow curves. At maximum finite strain the viscosity in the direction parallel and perpendicular to the layer was 2.3×10^{13} and 1.9×10^{13} Pa s, respectively (Table 1).

The difference between horizontal and vertical stresses was still higher (ca. 2 MPa) if the layer thickness, H_i, was set at 2.5 mm (Fig. 3f). Because of increased mechanical significance of the anhydrite layer, the pre-scribed stress limit (4.6 MPa) was reached in the horizontal direction (along the layer) already at $e_{Y=Z}=−17\%$. Thus, the experiment had to be stopped much earlier than in the other runs described above. At maximum finite strain the viscosity in the direction parallel and perpendicular to the layer was 2.2×10^{13} and 1.1×10^{13} Pa s, respectively.

3.2. Geometry of deformed halite matrix

A striking feature of sections cut parallel to the *X*-axis of the finite strain ellipsoid ($XY = XZ$ sections) is a fabric in the deformed matrix which results from the shape-preferred orientation (SPO) of both halite and anhydrite, the latter forming primary inclusions inside the halite matrix (Fig. 4a). Sections cut perpendicular to the *X*-axis are free from such a grain-shape fabric. Here the sections through halite crystals and anhydrite inclusions are almost circular (Fig. 4b). The impact of finite strain on the grain-shape fabric is obvious when comparing the *X*-parallel section of the sample with the thickest anhydrite layer ($H_i = 2.5$ mm, Fig. 5f) with the remaining samples (Fig. 5a–e). These samples show a finite strain ($e_x = 122\%$) that is three times higher than the strain of the sample with the thickest layer ($e_x = 44\%$). In the latter sample the degree of SPO of anhydrite inclusions is much lower than that in the samples subjected to $e_x = 122\%$.

A further striking feature of $XY = XZ$ sections of all samples undergoing higher finite strain is a healed fracture that is trending subperpendicular to the anhydrite layer (Fig. 5a–e). This healed fracture is present in the central part of the samples where it cuts through halite, but not always through anhydrite (Fig. 6a,d), although the latter was the more competent phase. All of these fractures are weakly folded and rarely displaced along shear planes which are oriented parallel to the *X*-axis. Given the fracture was initially straight, the longitudinal post-fracture strain produced by folding could be determined by retrofolding of the fracture using
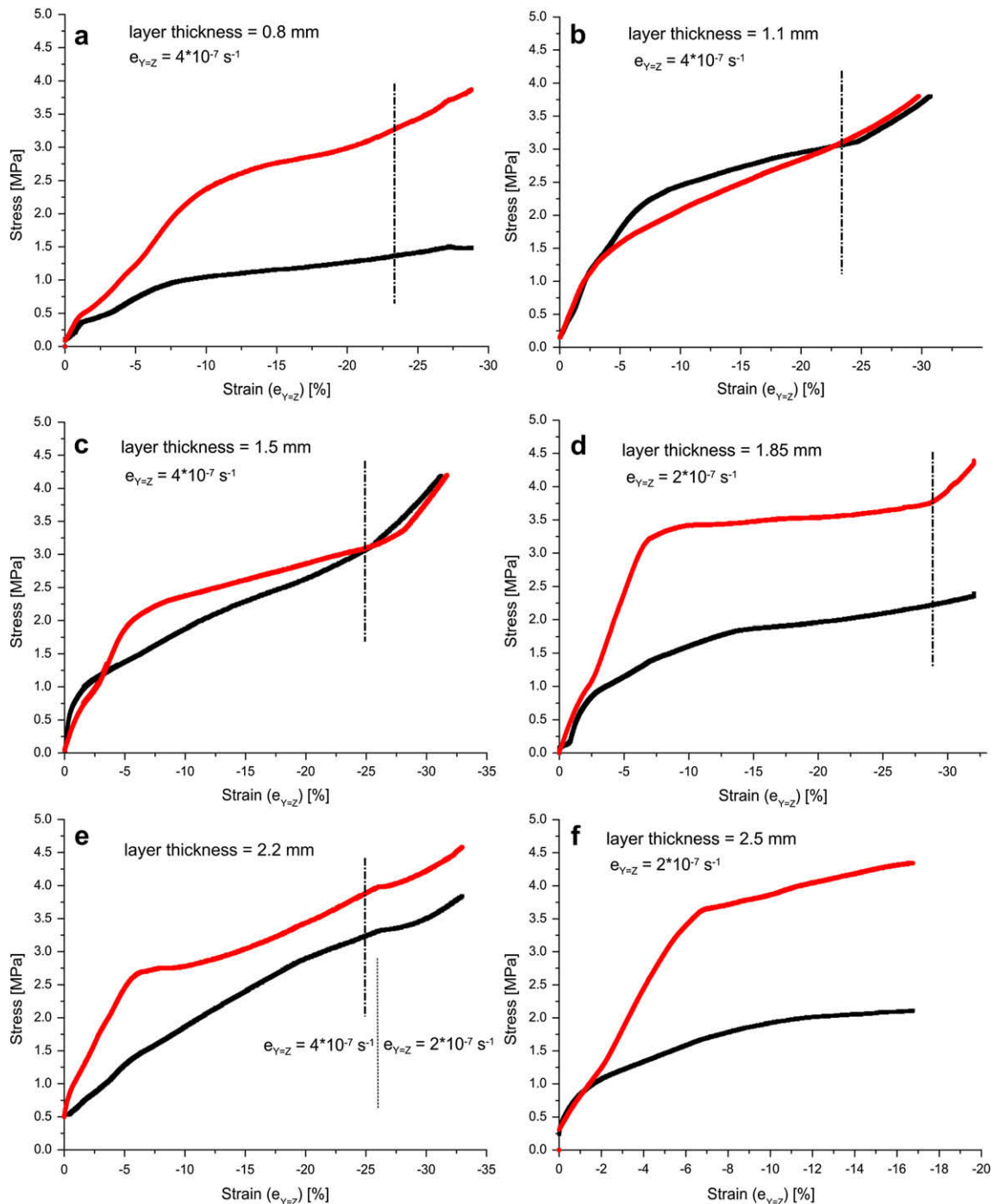
Fig. 3. Stress vs. strain plots of constrictional runs applied to composite samples of halite matrix (Asse halite, Na2SP) and single layer of Gorleben anhydrite at various thickness. Deformation temperature, $T = 345\ ^\circ C$. Strain rates are listed in diagrams. Note that strain rate was changed in (e). Black line shows vertical axis ($Y = Z$) perpendicular to layer. Red curve shows horizontal axis ($Y = Z$) parallel to layer. Vertical bold broken line indicates the strain at which the pervasive fracture has formed subperpendicular to the X-axis of the sample.

image analysis software. The amount of shortening in the direction perpendicular to the anhydrite layer is low reaching from −4 to −8% (Table 1).

3.3. Geometry of deformed anhydrite layer

The sections cut parallel to the X-axis of the finite strain ellipsoid and perpendicular to the layer show striking boudinage of the stiff anhydrite layer (Figs. 5a–f and 6a–d). The boudin patterns display

striking boundary effects as is obvious from CT images which are oriented parallel to the layer (Fig. 7a–f). In these CT images the deformed anhydrite layer is shown whereas the deformed halite matrix is not considered. Close to the X-parallel margins of the sample the width of boudins and/or necks is lower than in the central part. Along the free planes of the sample, which are trending perpendicular to the X-axis and which were not confined by the plates of the machine, the degree of boudinage is less strong than in the central part. Most of the boudins are not penetrative and are
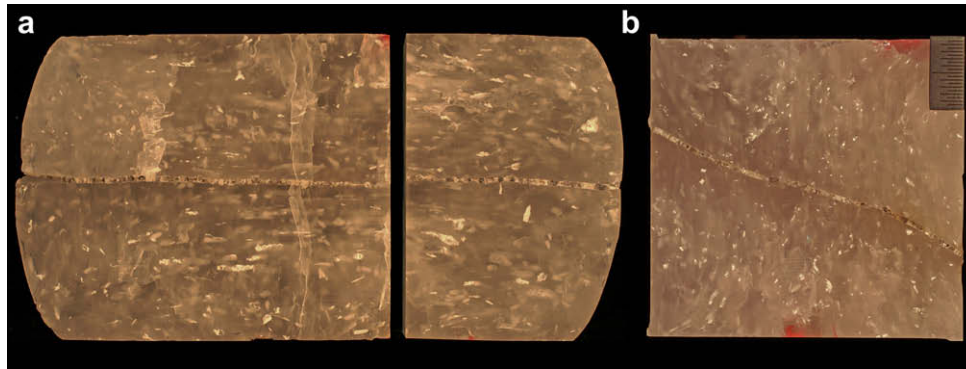
Fig. 4. Anhydrite layer in halite matrix deformed under bulk constriction at $T = 345\,°C$ and strain rate $= 4 \times 10^{-7}\,s^{-1}$, $H_i = 1.1$ mm, $e_x = 122\%$; $e_{Y=Z} = -33\%$. (a) Section cut parallel to the X-axis of the finite strain ellipsoid and perpendicular to the layer; vertical cut reflects the second section cut perpendicular to the X-axis (b). Note the large amount of small anhydrite inclusions the long axis of which is strongly oriented subparallel to the X-axis.

trending oblique to the principal strain axes. Some boudins show open folding with the fold axis being oriented subperpendicular to the layer. This holds particularly for cases where the layer is initially thin ($H_i < 2.0$ mm, Fig. 7a–c). Investigations of conventional sections cut parallel and perpendicular to the X-axis, respectively, suggest that the thickness of the boudins is almost the same like the thickness of the initial layer (Fig. 8a). Thus, the thickness of the layer remained nearly constant throughout the individual runs. It is difficult to explain why the CT images show a weak thickening in cases where the layer thickness is low ($H_i < 2$ mm), whereas the thickness of initially thicker layers decreased.

Statistic analyses of both conventional cuts ($XY = XZ$ sections) and CT images show an almost linear increase in boudin width (boudin wavelength) with layer thickness (Fig. 8c), whereas the number of boudins decreases almost linearly (Fig. 8d). The value of W_d (width of boudins divided by finite layer thickness) is almost the same within uncertainty ranging from ca. 0.5 to 2.5 (Fig. 8e).

Close-up views of $XY = XZ$ sections show the layer to be affected by fracture boudinage. Most of the fractures are oriented subperpendicular to the layer (Fig. 6a–d). In a few cases, however, there are fractures which are oriented oblique to the layer. The boudins are in a few cases asymmetric with respect to the X-axis (Fig. 6c).
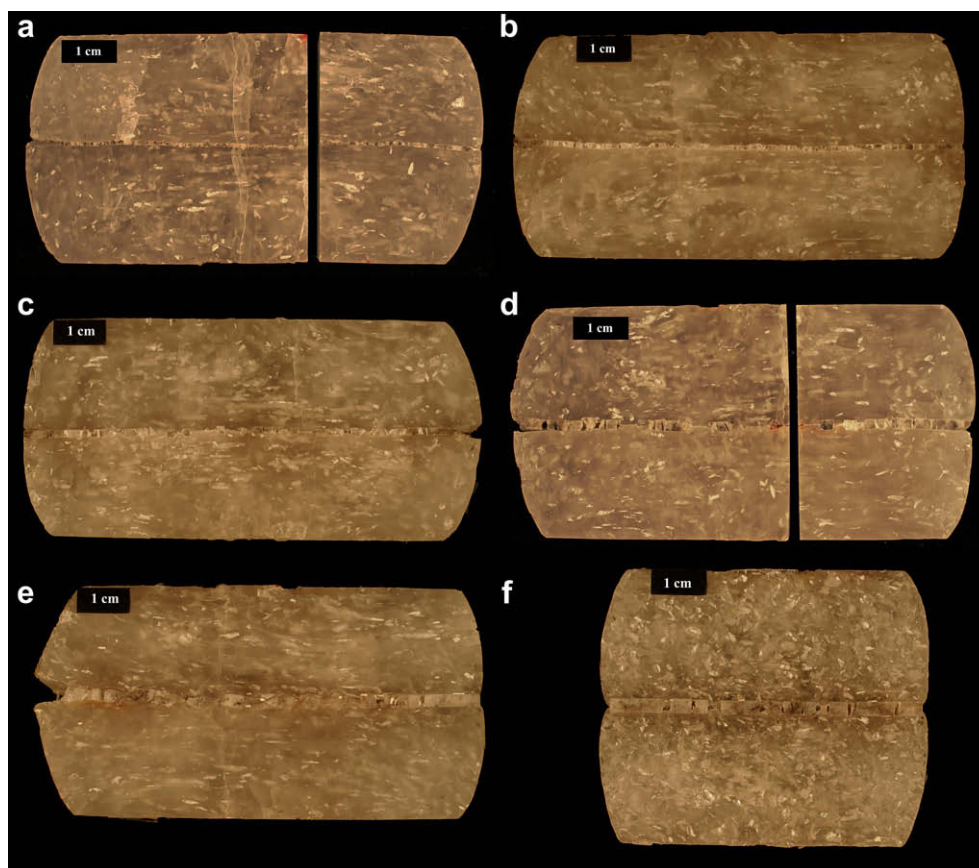
Fig. 5. Anhydrite layer in halite matrix deformed under bulk constriction at $T = 345\,°C$ and strain rate $= 2–4 \times 10^{-7}\,s^{-1}$. All sections cut parallel to the X-axis of the finite strain ellipsoid and perpendicular to the layer. (a) $H_i = 0.8$ mm, $e_x = 116\%$; $e_{Y=Z} = -32\%$; (b) $H_i = 1.1$ mm, $e_x = 122\%$; $e_{Y=Z} = -33\%$; (c) $H_i = 1.5$ mm, $e_x = 122\%$; $e_{Y=Z} = -33\%$; (d) $H_i = 1.85$ mm, $e_x = 116\%$; $e_{Y=Z} = -32\%$; (e) $H_i = 2.2$ mm, $e_x = 122\%$; $e_{Y=Z} = -33\%$; (f) $H_i = 2.5$ mm, $e_x = 44\%$; $e_{Y=Z} = -17\%$.
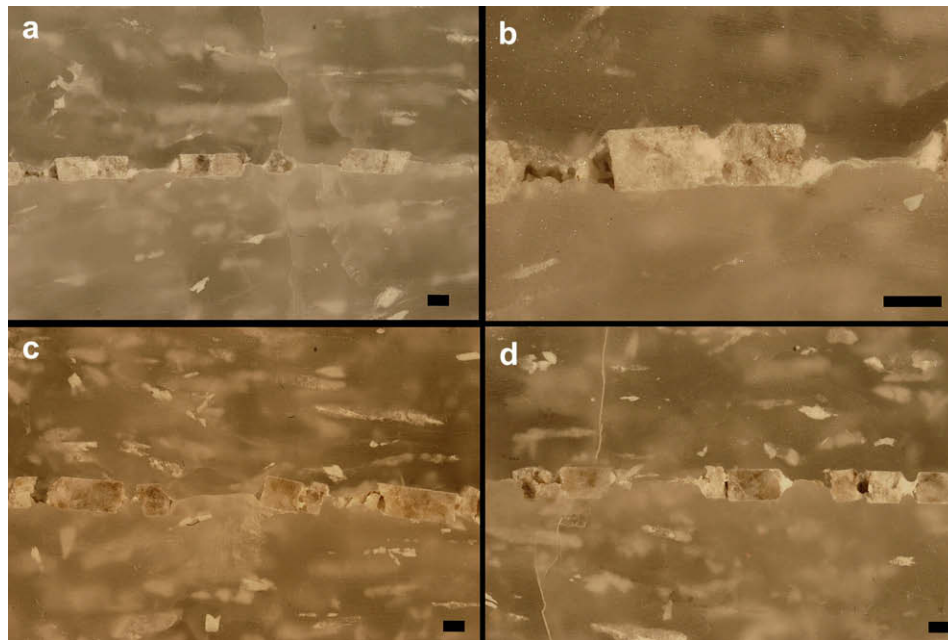
Fig. 6. Close-up view of deformed samples shown in Fig. 5. (a,b) initial thickness (H_i) of anhydrite layer = 1.1 mm. (c,d) H_i = 1.5 mm. Note that the necks between the anhydrite boudins are different in composition. Scale bar = 1 mm.

Most of the necks between the boudins are entirely filled with halite. However, in a few cases halite was not able to fill the neck completely. This holds particularly if $H_i > 2$ mm and for cases where the width of the fractures inside the anhydrite layer was small.

There is further evidence that some of the necks are filled with a white material (Fig. 6b,d).

In sections cut perpendicular to the X-axis the anhydrite layer shows weak folding (sensu Zulauf and Zulauf, 2005) and significant
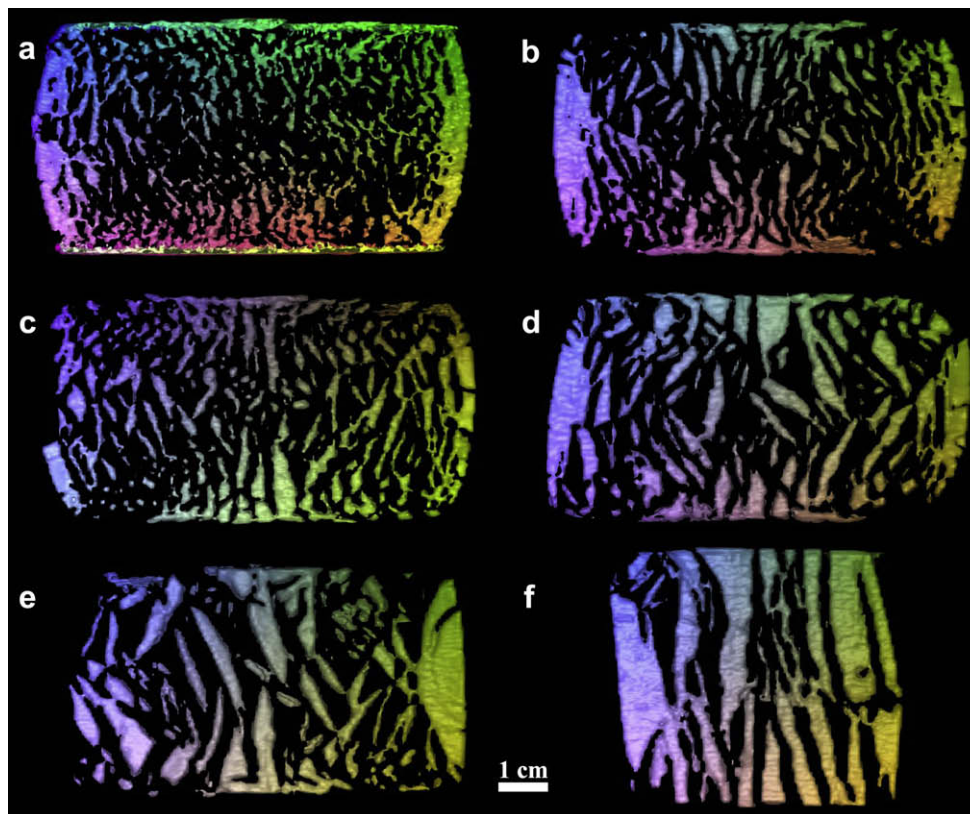
Fig. 7. CT images of anhydrite boudins deformed under bulk constriction at $T = 345\ °C$ and strain rate = $2–4 \times 10^{-7}\ s^{-1}$ in halite matrix (the latter not shown). View perpendicular to the X-axis of the finite strain ellipsoid and perpendicular to the layer. (a) $H_i = 0.8$ mm, $e_x = 116\%$; $e_{Y=Z} = -32\%$; (b) $H_i = 1.1$ mm, $e_x = 122\%$; $e_{Y=Z} = -33\%$; (c) $H_i = 1.5$ mm, $e_x = 122\%$; $e_{Y=Z} = -33\%$; (d) $H_i = 1.85$ mm, $e_x = 122\%$; $e_{Y=Z} = -33\%$; (e) $H_i = 2.2$ mm, $e_x = 122\%$; $e_{Y=Z} = -33\%$; (f) $H_i = 2.5$ mm, $e_x = 44\%$; $e_{Y=Z} = -17\%$.
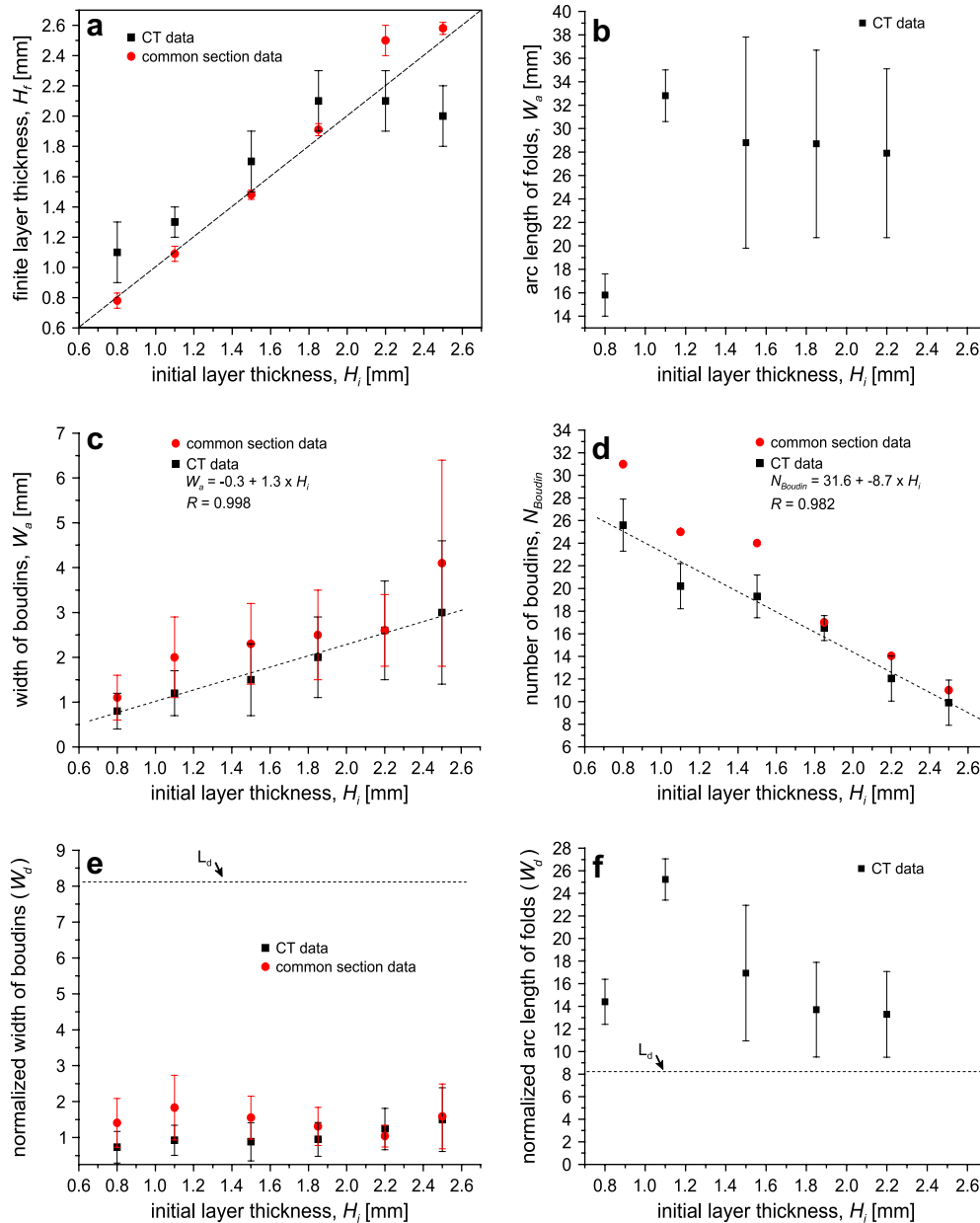
Fig. 8. Geometric data of anhydrite layer embedded in halite matrix deformed under bulk constriction with the layer parallel to X. Deformation temperature, $T = 345$ °C. Strain rate $= 2–4 \times 10^{-7}$ s^{-1}. Geometric parameters are plotted vs. initial layer thickness (H_i). Data shown have been obtained by Computer Tomography (CT) and by analysis of common sections cut parallel to X and perpendicular to the layer (c, d, e) and perpendicular to X and perpendicular to the layer (a, b, f). L_d = normalized initial wavelength calculated after Smith (1977). Finite strain ($e_{Y=Z}$) $= -32\%$ for initial layer thicknesses 0.8, 1.1, 1.5, and 2.2 mm. Finite strain ($e_{Y=Z}$) $= -17\%$ for initial layer thickness of 2.5 mm. Note that linear regression lines depicted in (c) and (d) are considering only the CT data. R = correlation coefficient.

drag at both ends due to friction along the boundaries between sample and plate (Figs. 9a–e and 10a–e). The rare folds have axes trending subparallel to the X-axis and display a large arc length (Fig. 8b). Some are kink folds showing sharp hinges, some of which are broken. The thickest layer ($H_i = 2.5$ mm), which underwent lower finite strain, is free from this type of folding (Figs. 9f, 10f). The low number of folds results in a large uncertainty of geometric data. Consequently, a clear relation between H_i and arc length of folds is not supported by the few data obtained (Fig. 8b).

4. Discussion

In the previous sections results of first experiments are presented which led to folding and boudinage of a single anhydrite

layer embedded in a weaker halite matrix. Although the deformed Gorleben anhydrite and Asse halite are natural rocks that were deposited in a saliniferous Permian basin, our experiments are not the first where natural rocks were subjected to folding. Fault-bend and fault-propagation folds were experimentally produced at room temperature and confining pressure using sandstone and limestone which were deformed in the brittle field (Chester et al., 1991). On the other hand, our studies imply – to our knowledge – the first thermomechanical experiments on 3D-folding *and* boudinage of a natural competent rock embedded in a natural incompetent matrix, the latter undergoing dislocation creep. Materials used in previous studies to model folding and boudinage under viscous or partly viscous conditions are largely restricted to rock analogues such as wet clay, wax or plasticine (e.g. Ramberg, 1955, 1961;
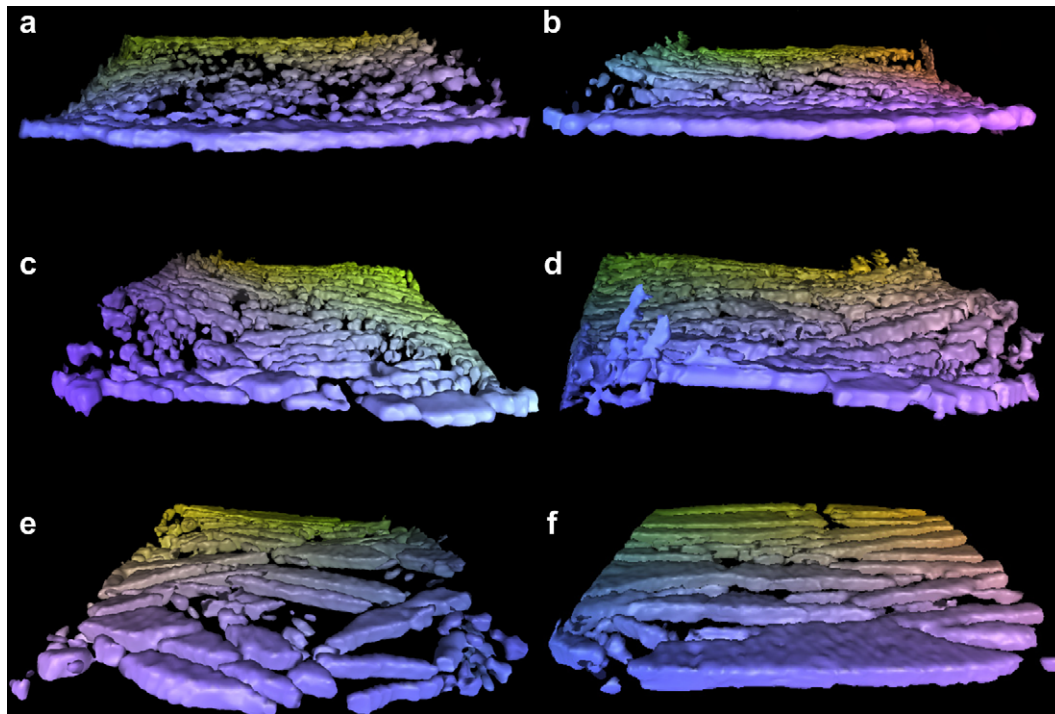
Fig. 9. CT images of anhydrite layer deformed under bulk constriction at $T = 345\,^{\circ}\mathrm{C}$ and strain rate $= 2$–$4 \times 10^{-7}\,\mathrm{s}^{-1}$ in halite matrix (the latter not shown). View subparallel to the X-axis of the finite strain ellipsoid and subparallel to the layer. (a) $H_i = 0.8$ mm, $e_x = 116\%$, $e_{Y=Z} = -32\%$; (b) $H_i = 1.1$ mm, $e_x = 122\%$, $e_{Y=Z} = -33\%$; (c) $H_i = 1.5$ mm, $e_{Y=Z} = -33\%$; (d) $H_i = 1.85$ mm, $e_x = 122\%$, $e_{Y=Z} = -33\%$; (e) $H_i = 2.2$ mm, $e_x = 122\%$, $e_{Y=Z} = -33\%$; (f) $H_i = 2.5$ mm, $e_x = 44\%$, $e_{Y=Z} = -17\%$.

Hudleston, 1973; Cobbold, 1975; Watkinson, 1975; Neurath and Smith, 1982; Abbassi and Mancktelow, 1992; Gosh et al., 1995; Grujic and Mancktelow, 1995; Tentler, 2001; Zulauf et al., 2003; Zulauf and Zulauf, 2005). A layer of synthetic rock salt embedded in plasticine matrix was folded experimentally by Gairola and Kern (1984).

The new deformation rig is capable to deform relatively large samples of halite and anhydrite at elevated constant temperature ($T_{\mathrm{max}} = 345\,^{\circ}\mathrm{C}$) and differential stress ($\sigma_{\mathrm{max}} = 4.6$ MPa), but without imposing a confining pressure. In each experiment carried out in the present study two surfaces of the cuboid samples, which are oriented perpendicular to the X-axis of the finite strain ellipsoid, were unconfined. This is in contrast to natural environments.

As has been expected from previous experimental studies on the mechanical behavior of halite, under the conditions used in the present study the Asse halite behaved viscously. The flow behavior
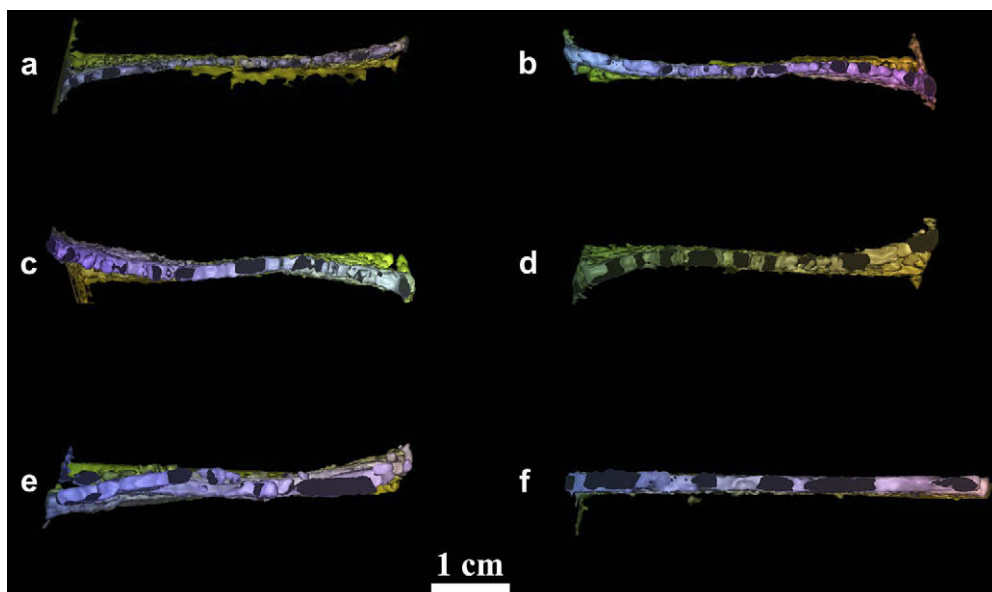
Fig. 10. CT images of anhydrite layer deformed under bulk constriction at $T = 345\,^{\circ}\mathrm{C}$ and strain rate $= 2$–$4 \times 10^{-7}\,\mathrm{s}^{-1}$ in halite matrix (the latter not shown). View is parallel to the X-axis of the finite strain ellipsoid and parallel to the layer. (a) $H_i = 0.8$ mm, $e_x = 116\%$, $e_{Y=Z} = -32\%$; (b) $H_i = 1.1$ mm, $e_x = 122\%$, $e_{Y=Z} = -33\%$; (c) $H_i = 1.5$ mm, $e_x = 122\%$, $e_{Y=Z} = -33\%$; (d) $H_i = 1.85$ mm, $e_x = 122\%$, $e_{Y=Z} = -33\%$; (e) $H_i = 2.2$ mm, $e_x = 122\%$, $e_{Y=Z} = -33\%$; (f) $H_i = 2.5$ mm, $e_x = 44\%$, $e_{Y=Z} = -17\%$.

of synthetic and natural polycrystalline halite has been investigated by numerous experimental studies. Work carried out on *synthetic rock salt* was conducted at $T = 20$–$780\,°C$, $P_{conf} = 0$–$200\,MPa$, and $\dot{e} =$ down to $10^{-8}\,s^{-1}$ (e.g. Heard, 1972; Franssen and Spiers, 1990; Franssen, 1994). *Natural rock salt* has been investigated under the following conditions: $T = 20$–$250\,°C$, $P_{conf} =$ up to $30\,MPa$, and $\dot{e} =$ down to $10^{-10}\,s^{-1}$ (e.g. Carter and Hansen, 1983; Wawersik and Zeuch, 1986; Carter et al., 1993; Peach et al., 2001). Carter et al. (1993) revealed a major change in flow behavior with increasing stress and strain rate. This change in flow behavior is ascribed to a change in rate-limiting mechanisms from cross-slip of screw dislocations to the climb of edge dislocations (Carter et al., 1993). Franssen (1994) has separated two temperature-dependent flow fields which are related to different modes of dislocation creep. Under the deformation conditions applied in the present study ($T = 345\,°C$, $\dot{e} = 10^{-7}\,s^{-1}$, $\sigma_{max} = 4.6\,MPa$, $P_{conf} = 0$), dry halite should be deformed by climb-controlled dislocation creep (subgrain rotation recrystallization) with strain hardening resulting in a stress exponent, n, of ca. 6 and an apparent viscosity of ca. $3 \times 10^{13}\,Pa\,s$ (Franssen, 1994).

In contrast to halite, the anhydrite of the Gorleben borehole was deformed in the brittle field as is documented by fracture boudinage. The mechanical behavior of anhydrite has been investigated during several studies at various temperatures, strain rates and grain sizes (Müller and Siemes, 1974; Müller et al., 1981; Ramez, 1976a, 1976b; Dell'Angelo and Olgaard, 1995; Heidelbach et al., 2001). Mixtures of anhydrite and halite have been deformed and investigated by Ross et al. (1987).

If deformation occurs at low temperature, twinning on the {101} planes is the major deformation mechanism of anhydrite, and the <100> axis is aligned subparallel to the principal compression axis (σ_1). Fine-grained anhydrite samples become strongly temperature and strain-rate dependent at $T > 300\,°C$. Experiments performed by Dell'Angelo and Olgaard (1995) at $T = 400$–$800\,°C$, $\dot{e} = 10^{-3}$–$10^{-6}\,s^{-1}$, and confining pressures of 150–300 MPa yielded a stress exponent, n, at ca. 5. Steady-state flow at elevated temperatures and low stresses was found to correlate with the onset of dynamic recrystallization by grain and twin boundary migration and subgrain rotation (Müller et al., 1981). At $T = 300\,°C$ and $\dot{e} = 10^{-7}$–$10^{-6}\,s^{-1}$ (conditions which are similar to those of the present study) anhydrite should be deformed in the brittle–plastic regime that is characterized by twinning, kinking and microfracturing (Müller et al., 1981; Ross et al., 1987). The viscosities at these conditions are between 10^{14} and $10^{15}\,Pa\,s$. Based on the rheological data listed above, the viscosity ratio, m, between anhydrite layer and halite matrix is estimated at ca. 27.

As most of the experiments were carried out at constant strain rate, and stress was continuously measured while the sample was deformed, we can calculate the in-situ viscosity along the horizontal and vertical directions, respectively. The maximum viscosity obtained in the present study reaches from 4×10^{12} to $2 \times 10^{13}\,Pa\,s$ (perpendicular to the layer) and 1×10^{13} to $2 \times 10^{13}\,Pa\,s$ (parallel to the layer) (Table 1). These viscosities are much lower than those of anhydrite but are compatible with the data obtained for halite by Franssen (1994, see above), meaning that the anhydrite layer did not significantly affect the viscosity of the sample, even in those cases where the layer was thick.

However, a certain but weak impact of the anhydrite layer on the mechanical behavior of the deforming sample is indicated by the stress–strain curves. In cases where $H_i >$ ca. 1.5 mm, the anhydrite layer was mechanically active not only at low finite strain but throughout the entire run as is indicated by the higher stresses and by the later onset of plastic yielding in the direction parallel to the layer. There is, on the other hand, a further impact on the viscosity if a strong SPO is present in the initial halite sample as has been shown by recent experiments using pure Asse halite (Zulauf, in preparation). These experiments have shown that the stress parallel to the planar grain-shape fabric is higher than the stress perpendicular to this fabric. This observation might explain the unexpected stress–strain curves in the experiment where H_i was set at 0.8 mm. In the latter case the anhydrite layer should not have caused the strong difference in stress along the two principal directions (parallel and perpendicular to the layer) as the layer is too thin. In this particular case the striking difference in stress, recorded parallel and perpendicular to the layer, should result from the grain-shape fabric of the halite matrix which – in comparison to the other samples – was relatively strong in the starting sample of Asse halite and was oriented subparallel to the anhydrite layer.

A further interesting feature in most of the stress–strain plots is a striking increase in strain hardening at $e_{Y=Z} = -25$ to -30%. We assume that this increase in strain hardening reflects a change in the crystallographic slip systems which are active in halite during dislocation creep. The strong strain hardening at advanced state of finite strain should have caused the pervasive transient fracture which cuts through almost all of the samples in the direction subperpendiucular to the X-axis. As this fracture is lacking in the sample with $H_i = 2.5\,mm$, which underwent a much lower degree of strain ($e_{Y=Z} = -17\%$, Fig. 3f), we assume that the X-perpendicular pervasive fracture is a late feature that developed at advanced finite strain. This assumption is supported by the fact that the amount of viscous shortening of the fracture due to folding was low reaching from 4 to 8% (Table 1). The pre-fracture ductile strain (i.e. the strain imposed before the fracture was opened) is calculated by subtracting the amount of post-fracture ductile strain from the finite strain of the individual samples. When depicting the values of pre-fracture ductile strain in the stress–strain plots (see vertical bold broken line in Fig. 3a–e), it is obvious that most of the X-perpendicular fractures developed during the phase of elevated strain hardening which affected most of the deformed samples.

Of particular interest in the present study is the geometry of the deformed anhydrite layer and the fabric inside the halite matrix. In the starting samples of Asse halite the small inclusions of anhydrite did not show any SPO. The experiments have shown that pure constriction up to a finite strain of $e_x = 122\%$ led to a strong prolate fabric in the halite matrix that is documented by the SPO of the small anhydrite inclusions. A similar linear grain-shape fabric portrayed by disseminated anhydrite and spindle-shaped aggregates of anhydrite has been described from the Grand Saline dome where the lineation is axial to the steeply plunging curtain folds (Balk, 1949).

The anhydrite layer shows a complex deformation geometry. There is a strong boundary effect resulting from friction between the sample and the plates of the machine. This effect, however, is vanishing at a distance of ca. 0.5 cm from the margin towards the centre of the sample, meaning that the central part of the sample shows patterns reflecting almost continuum-style deformation. The 3D-geometry of the deformed anhydrite layer could not be fully delineated using conventional cuts. CT analysis, on the other hand, has proved to be a robust tool to image the geometry of the deformed layer in 3D without destroying the sample. The material parameters of halite and anhydrite, which are critical for carrying out CT analysis (such as density contrast), are ideal for using a medical CT without changing the analytical parameters adjusted for medical purposes. In most cases where geometric data have been obtained using both conventional cuts and CT, the data are the same within uncertainty. However, if the thickness of the anhydrite layer is less than ca. 1 mm, the resolution of a common medical CT scanner is too low to image the deformed layer in detail. In these cases the folds and boudins should be investigated using a Micro-CT scanner.

The geometry of the deformed anhydrite layer and the geometry of folded plasticine layers, are similar to a certain extent, given the plasticine layers also underwent pure constriction inside a weaker plasticine matrix and the viscosity contrast between matrix and layer, m, is much larger than 5 (Kobberger and Zulauf, 1995; Zulauf et al., 2003). The CT analyses of incrementally deformed plasticine samples suggest that both folds with axes subparallel to the X-axis and boudins with the long axis perpendicular to the X-axis develop simultaneously under pure constriction. The growth rate of both instabilities is similar (Zulauf and Zulauf, 2005). This situation is not given in the present study. In the anhydrite layer the growth rate of boudins is much higher than the growth rate of the folds. In natural salt diapirs there are curtain folds which are common structural elements inside the stems of the diapirs (see references above). In the anhydrite layer of the present study, however, curtain-type folds do hardly occur. Moreover, the folds in the plasticine samples show curved hinges, whereas the hinges in the anhydrite layer are either sharp (kink folds) or are broken reflecting brittle behavior.

Theories of buckle folding in non-linear viscous materials suggest the initial wavelength of buckle folds and boudins to be the same. This assumption applies to plasticine samples where both type of instabilities developed simultaneously under bulk constriction (Zulauf and Zulauf, 2005). The geometrical and rheological parameters of these instabilities are related by the following equation (Fletcher, 1974; Smith, 1977, 1979):

$$L_d \approx 3.46 \left(n_2^{1/6} / n_1^{1/3} \right) (\eta_1/\eta_2)^{1/3} \qquad (1)$$

where L_d is the theoretical wavelength/thickness ratio, and n_1, η_1 and n_2, η_2 are the stress exponents and the effective viscosities in the flow laws for layer and matrix, respectively. Inserting the rheological data listed above into equation (1) results in a normalized initial wavelength, L_d, for folds and boudins of 8.1. The actual values of the normalized wavelength of anhydrite folds (W_d), however, range from ca. 10 to 27 when considering the uncertainties (Fig. 8f). The large difference between W_d and L_d probably results from the fact that the folds are not real buckle folds inside viscous material, but are kink folds, which developed in the brittle to brittle–viscous field and thus cannot be described by equation (1). The brittle behavior of the anhydrite layer might also explain why the folds with axes parallel to the X-axis are rare. A further reason for the scarcity of these folds in anhydrite could be the lack of confining pressure.

The anhydrite boudins are definitely fracture boudins as is shown by the sharp and straight boundary between boudin and neck. This boundary is oriented perpendicular to the layer. The dimensionless value of W_d (width of boudins divided by finite layer thickness) is 1.5 ± 1.0 and thus much below the L_d value calculated using equation (1) (Fig. 8e). Also in this case, the large difference between W_d and L_d can be explained by the brittle behavior of the layer. However, in contrast to the folds, the W_d value of the boudins shows a much lower scatter and uncertainty. Incremental experiments using plasticine samples have shown that bulk constriction results in drawn boudins, the width of which does not significantly change with finite strain (Zulauf and Zulauf, 2005). If this also applies to halite–anhydrite samples, the W_d value of the anhydrite boudins should be a reliable geometrical parameter which – independent of the finite strain of the sample – can be used to reveal constrictional fracture boudinage.

A further particular characteristic of the boudins is shown by a linear regression analysis of W_a vs. H_i, which yielded the following equation, based on CT data (Fig. 8c):

$$W_a = -0.3 + 1.3 \times H_i \qquad (2)$$

The regression coefficient, $R = 0.998$, shows a good linear fit of the data. When using the W_a values obtained by analyses of common sections, the linear fit of W_a vs. H_i is worse ($R = 0.916$).

A linear relationship is also given between the number of boudins, N_{Boudin}, and the layer thickness. A linear regression analysis yielded the following equation, based on CT data (Fig. 8d):

$$N_{Boudin} = 31.6 + -8.7 \times H_i \qquad (3)$$

Also in this case the regression coefficient, $R = 0.982$, shows a good linear fit of the data.

The long axis of most of the boudin stripes is not perpendicular but oblique to the X-axis as is indicated by the CT images (Fig. 7). Some of the boudin stripes are weakly folded with fold axis being oriented subperpendicular to the layer. Incremental studies using plasticine as rock analogue have shown that this type of fold develops at advanced state of strain due to lateral shortening of the previously formed boudin stripes. For this reason these folds, with axis subperpendicular to the layer, are termed D_2 folds, whereas the curtain-type folds with axis parallel to the X-axis are termed D_1 folds (Zulauf and Zulauf, 2005). The boudin stripes were superposed by the D2-folding and thus show a more or less oblique position with respect to the principal strain axes. As D2-folding proceeds, some of the boudins rotate progressively towards the X-axis of the finite strain ellipsoid. If the rotation is sufficient for the boudin stripes to become subparallel to the X-axis, the boudins are in the orientation where they may be affected by further necking resulting in D_2 boudinage (Zulauf and Zulauf, 2005). This type of boudinage, however, is rare or absent in the present samples.

Thus, at high strain magnitudes pure constriction causes complex deformation pattern, if a brittle to brittle–ductile anhydrite layer is embedded in a viscous matrix of halite with most of the boudin stripes trending oblique to the X-axis. In the present case of composite halite–anhydrite samples or in cases of rock analogues, the analysis of these three-dimensional structures is possible using CT images. In natural environments, however, these structures can be identified only in those cases where rock salt is well exposed in three dimensions.

It is yet not clear if the white material inside few of the boudin necks results from syn- to late-kinematic mineralization within open pore space of the neck. The fluid from which such a mineralization may have precipitated could have been available from the numerous fluid inclusions in halite and anhydrite. The relatively high temperature and the viscosity data presented above, however, are not consistent with deformation under wet conditions resulting in solution–precipitation creep.

5. Conclusions and open questions

The present study has shown that constriction in stems of salt diapirs may result in complex 3D deformation patterns if an anhydrite layer is embedded in halite, with the layer being oriented parallel to the X-axis of the finite strain ellipsoid. Such structures are difficult to analyze without using specific techniques such as CT which does not only show the structures in 3D but can also be used without destroying the sample.

A major result of the present study is that folds, with axes parallel to the X-axis, are much scarcer than boudins. This observation is in contrast to nature, where curtain folds are common structures in stems of salt diapirs, and is in contrast to the results obtained from constrictional experiments applied to non-linear viscous plasticine. The reason for the different deformation pattern of composite halite–anhydrite samples on the one hand and plasticine samples on the other hand is probably the different behavior

of the competent layer. In cases of plasticine this layer behaved largely viscous, whereas under the conditions of the present study the anhydrite layer behaved by brittle fracturing. In natural environments there is an additional confining pressure that is lacking in the present experiments. Moreover, the matrix of halite may deform by solution–precipitation creep or by combined solution–precipitation and dislocation creep.

In order to constrain the deformation mechanisms of anhydrite and halite used in the present study, microstructural and textural analyses of irradiated samples will be carried out. The results of these studies will also help to find out the reason for the dramatic strain hardening in halite at advanced finite strain and to determine the type of mineral which grew in the necks of the boudins.

The results presented in the present paper are of interest not only for rock salt but are also important for other constrictional environments where a brittle layer is deformed in a viscous matrix. Such conditions could be present in subduction zones where a rigid layer of quartzite or dolomite is constrictionally deformed inside a viscous pelitic matrix undergoing very low-grade metamorphism (e.g. Zulauf et al., 2002).

Acknowledgements

References

Abbassi, M.R., Mancktelow, N.S., 1992. Single layer buckle folding in non-linear materials-I. Experimental study of fold development from an isolated initial perturbation. Journal of Structural Geology 14, 85–104.

Balk, R., 1949. Structure of Gand Saline dome, Van Zandt County, Texas. AAPG Bulletin 33, 1791–1829.

Balk, R., 1953. Salt structure of Jefferson Island salt dome, Iberia and Vermilion Parishes, Lousiana. AAPG Bulletin 37, 2455–2474.

Bauerle, G., Bornemann, O., Mauthe, F., Michalzik, D., 2000. Origin of stylolites in Upper Permian Zechstein anhydrite (Gorleben Salt Dome, Germany). Journal of Sediment Research 70 (3), 726–737.

Brokmeier, H.G., 1983. Texturuntersuchungen an natürlichen und experimentell verfestigten Halitgesteinen mit Neutronen- und Wolfram Kα Strahlung. Ph.D. thesis, Technical University, Clausthal Zellerfeld, Germany, 160 pp.

Carter, N.L., Hansen, F.D., 1983. Creep of rocksalt. Tectonophysics 92, 275–333.

Carter, N.L., Horseman, S.T., Russell, J.E., Handin, J., 1993. Rheology of rocksalt. Journal of Structural Geology 15, 1257–1271.

Chemia, Z., Koyi, H., 2008. The control of slat supply on entrainment of an anhydrite layer within a salt diapir. Journal of Structural Geology 30, 1192–1200.

Chemia, Z., Koyi, H., Schmeling, H., 2008. Numerical modelling of rise and fall of a dense layer in salt diapirs. Geophysical Journal International 172, 798–816.

Chester, J.S., Logan, J.M., Spang, J.H., 1991. Influence of layering and boundary conditions on fault-bend and fault-propagation folding. GSA Bulletin 103, 1059–1072.

Cobbold, P.R., 1975. Fold propagation in single embedded layers. Tectonophysics 27, 333–351.

Davison, I., Alsop, G.I., Blundell, D.J., 1996a. Salt tectonics: some aspects of deformation mechanism. In: Alsop, G.I., Blundell, D.J., Davison, I. (Eds.), Salt Tectonics, vol. 100. Geological Society, London, pp. 1–10. Special Publications.

Davison, I., Bosence, D., Alsop, G.I., Al-Aawah, M.H., 1996b. Deformation and sedimentation around active Miocene salt diapirs on the Tihama Plain, northwest Yemen. In: Alsop, G.I., Blundell, D.J., Davison, I. (Eds.), Salt Tectonics, vol. 100. Geological Society, London, pp. 23–39. Special Publications.

Dell'Angelo, L.N., Olgaard, D.L., 1995. Experimental deformation of fine-grained anhydrite: evidence for dislocation and diffusion creep. Journal of Geophysical Research 100B, 15425–15440.

Escher, B.G., Kuenen, 1929. Experiments in connection with salt domes: Leidsche Geologiese Meddelanden, 3, 151–182.

Fletcher, R.C., 1974. Wavelength selection in the folding of a single layer with power-law rheology. American Journal of Science 274, 1029–1043.

Franssen, R.C.M.W., 1994. The rheology of synthetic rocksalt in uniaxial compression. Tectonophysics 233, 1–40.

Franssen, R.C.M.W., Spiers, C.J., 1990. Deformation of polycrystalline salt in compression and in shear at 250–350 °C. In: Knipe, R.J., Rutter, E.H. (Eds.), Deformation Mechanisms, Rheology and Tectonics, vol. 45. Geological Society, London, pp. 201–213. Special Publication.

Gairola, V.K., Kern, H., 1984. Microstructure and texture in experimentally folded single-layer rock salt. Journal of Structural Geology 6, 201–213.

Gosh, S.K., Khan, D., Sengupta, S., 1995. Interfering folds in constrictional deformation. Journal of Structural Geology 17, 1361–1373.

Grujic, D., Mancktelow, N.S., 1995. Folds with axes parallel to the extension direction: an experimental study. Journal of Structural Geology 17, 279–291.

Hudleston, P.J., 1973. An analysis of single layer folds developed experimentally in viscous media. Tectonophysics 16, 189–214.

Hartwig, G., 1925. Praktisch-geologische Beschreibung des Kalisalzbergwerkes 'Rössing-Barnten' bei Hildesheim. Jahresberichte Niedersächsischer Geologischer Verein 17, 1–74.

Heard, H.C., 1972. Steady state flow in polycrystalline halite at pressures of 2 Kilobars. In: Heard, H.C., Borg, I.Y., Carter, N.L., Raleigh, C.B. (Eds.), Flow and Fracture of Rocks. Geophysical Monograph Series 16. Am. Geophys. Union, pp. 191–209.

Heidelbach, F., Stretton, I.C., Kunze, K., 2001. Texture development of polycrystalline anhydrite experimentally deformed in torsion. International Journal of Earth Sciences 90, 118–126.

Hoy, R.B., Foose, R.M., O'Neill, B.J., 1962. Structure of Winnfield salt dome, Winn Parish, Louisiana. AAPG Bulletin 46, 1444–1459.

Jackson, M.P.A., 1995. Retrospective salt tectonics. In: Jackson, M.P.A., Roberts, D.G., Snelson, S. (Eds.), Salt Tectonics: a Global Perspective, vol. 65. AAPG Memoir, pp. 1–28.

Jackson, M.P.A., Schultz-Ela, D.D., Hudec, M.R., Watson, I.A., Porter, M.L., 1998. Structure and evolution of Upheaval Dome: a pinched-off salt diapir. GSA Bulletin 110, 1547–1573.

Jackson, M.P.A., Talbot, C.J., 1987. Anatomy of mushroom shaped diapirs. Journal of Structural Geology 11, 211–230.

Kobberger, G., Zulauf, G., 1995. Experimental folding and boudinage under pure constrictional conditions. Journal of Structural Geology 17, 1055–1063.

Koyi, H.A., 2001. Modeling the influence of sinking anhydrite blocks on salt diapirs targeted for hazardous waste disposal. Geology 29, 387–390.

Lotze, F., 1957. Steinsalz und Kalisalze I. Gebrüder Bornträger, Berlin, 465 pp.

Müller, P., Siemes, H., 1974. Festigkeit, Verformbarkeit und Gefügeregelung von Anhydrit – Experimentelle Stauchverformung unter Manteldruck bis 5 kbar bei Temperaturen bis 300 °C. Tectonophysics 23, 105–127.

Müller, W.H., Schmid, S.M., Briegel, U., 1981. Deformation experiments on anhydrite rocks of different grain sizes: rheology and microfabric. Tectonophysics 78, 527–543.

Neurath, C., Smith, R.B., 1982. The effect of material properties on growth-rates of folding and boudinage: experiments with wax models. Journal of Structural Geology 4, 215–229.

Peach, C.J., Spiers, C.J., Trimby, P.W., 2001. Effect of confining pressure on dilatation, recrystallization, and flow of rock salt at 150 °C. Journal of Geophysical Research 106 (B7), 13315–13328.

Posepny, F., 1871. Studien aus dem Salinargebiete Siebenbürgens. Jahrbuch der Kaiserlich-Königlichen Reichsanstalt 21, 123–186.

Ramberg, H., 1955. Natural and experimental boudinage and pinch-and-swell structures. Journal of Geology 63, 512–526.

Ramberg, H., 1961. Contact strain and folding instability of a multilayered body under compression. Geologische Rundschau 51, 405–439.

Ramberg, H., 1981. Gravity, deformation and the earth's crust, second ed. Academic Press, London, 452 pp.

Ramez, M.R.H., 1976a. Mechanisms of intragranular gliding in experimentally deformed anhydrite. Neues Jahrbuch für Mineralogie, Abhandlungen 127, 311–329.

Ramez, M.R.H., 1976b. Fabric changes in experimentally deformed anhydrite rocks. Neues Jahrbuch für Mineralogie, Abhandlungen 128, 89–113.

Ramsay, J.G., Huber, I.H., 1987. The Techniques of Modern Structural Geology, Volume 2: Folds and Fractures. London: Academic Press.

Rogers, G.S., 1918. Intrusive origin of Gulf Coast salt domes. Economic Geology 13, 447–485.

Ross, J.V., Bauer, S.J., Hansen, F.D., 1987. Textural evolution of synthetic anhydrite-halite mylonites. Tectonophysics 140, 307–326.

Schenk, O., Urai, J.L., 2004. Microstructural evolution and grain boundary structure during static recrystallization in synthetic polycrystals of Sodium Chloride containing saturated brine. Contributions to Mineralogy and Petrology 146, 671–682.

Skrotzki, W., Welch, P., 1983. Development of texture and microstructure in extruded ionic polycrystalline aggregates. Tectonophysics 99, 47–61.

Sherwin, J.-A., Chapple, W.M., 1968. Wavelengths of single layer folds. A comparison between theory and observation: American Journal of Science 266, 167–178.

Smith, R.B., 1977. Formation of folds, boudinage, and mullions in non-Newtonian materials. Geological Society of America Bulletin 88, 312–320.

Smith, R.B., 1979. The folding of a strongly non-Newtonian layer. American Journal of Science 279, 272–287.

Stier, K., 1915. Strukturbild des Benther Salzgebirges. Jahresberichte Niedersächsischer Geologischer Verein, Hannover 8, pp. 1–15.

Stille, H., 1925. The upthrust of the salt masses of Germany. AAPG Bulletin 9, 417–441.

Talbot, C.J., Jackson, M.P.A., 1987. Internal kinematics of salt diapirs. AAPG Bulletin 71, 1086–1093.

Tentler, T., 2001. Experimental study of single layer folding in nonlinear materials. In: Koyi, H.A., Mancktelow, N.S. (Eds.), Tectonic Modeling: A Volume in Honor of Hans Ramberg, vol. 193. Geological Society of America Memoir, pp. 89–100.

Torrey, P.D., Fralich, C.E., 1926. An experimental study of the origin of salt domes. Journal of Geology 34, 224–234.

Trusheim, F., 1960. Mechanism of salt migration in northern Germany. Bulletin of American Association Petroleum Geologists 44, 1519–1540.

Urai, J.L., Spiers, C.J., Peach, C.J., Franssen, R.C.M.W., Liezenberg, J.L., 1987. Deformation mechanisms operating in naturally deformed halite rocks as deduced from microstructural investigations. Geologie Mijnbouw 66, 165–176.

Watkinson, A.J., 1975. Multilayer folds initiated in bulk plane strain, with the axis of no change perpendicular to the layering. Tectonophysics 28, T7–T11.

Wawersik, W.R., Zeuch, D.H., 1986. Modelling and mechanistic interpretation of creep of rock salt below 200 °C. Tectonophysics 121, 125–152.

Zirngast, M., 1996. The development of the Gorleben salt dome (northwest Germany) based on quantitative analysis of peripheral sinks. In: Alsop, G.I., Blundell, D.J., Davison, I. (Eds.), Salt Tectonics, vol. 100. Geological Society, London, pp. 203–226. Special Publications.

Zulauf, G., Kowalczyk, G., Petschick, R., Schwanz, S., Krahl, J., 2002. The tectonometamorphic evolution of high-pressure low-temperature metamorphic rocks of eastern Crete, Greece: constraints from microfabrics, strain, illite crystallinity and paleostress. Journal of Structural Geology 24, 1805–1828.

Zulauf, G., Zulauf, J., Hastreiter, P., Tomandl, B., 2003. A deformation apparatus for three-dimensional coaxial deformation and its application to rheologically stratified analogue material. Journal of Structural Geology 25, 469–480.

Zulauf, J., Zulauf, G., 2005. Coeval folding and boudinage in four dimensions. Journal of Structural Geology 27, 1061–1068.